Cartagena, Hernando-Pérez et al

Mapping *in vitro* local material physical properties of intact and disrupted virions at high resolution using multi-harmonic atomic force microscopy

In this supplementary material we provide additional information with respect to the following items:

A. Tip-sample interaction forces on a virus
B. Theory of multi-harmonic imaging and spectroscopy
C. Comparison of material properties extracted from multi-harmonic method vs. static force-distance curve
D. Data on additional viruses
E. Preparation of figures in the main text and supplement

A. Tip-sample interaction forces on a virus

A typical static Force (F_{ts}) vs. indentation ($\delta = -d$) curve on top of a ϕ29 virion in buffer solution is shown in Fig. S1a. The different constituents of F_{ts} include the elastic resistance of the virus and the associated hydration/solvation shell and the Derjaguin-Landau-Verwey-Overbeek (DLVO) forces (F_{DLVO}) which consist of electrostatic forces (F_{Elec}) and van der Waals forces (F_{VdW}). Because the buffer solution contains a mixture of monovalent and divalent ions it is difficult to estimate theoretically the Debye length on the virions. Instead, from experimental force-distance curves we have estimated that the Debye length on the virions λ_D is 2-4 nm.

Prior studies of viral mechanics have established (1, 2) that the tip-induced elastic deformation of the capsid shell together with its hydration/solvation layer (prior to buckling or damage) can be represented as a linear spring of constant $k_{elastic}$. On the other hand, the force gradient associated with $F_{ts,DLVO}$ is denoted as k_{DLVO} which is nonlinear and depends on d.

The effective repulsive force gradient k_{eff} can be considered to arise from two "springs" in series, the linear $k_{elastic}$ and the nonlinear k_{DLVO} i.e. $\frac{1}{k_{eff}} = \frac{1}{k_{DLVO}} + \frac{1}{k_{elastic}}$. At large "indentations" (forces > 500 pN) gradients due to k_{DLVO} are large compared to $k_{elastic}$ and $k_{eff} \sim k_{elastic}$. However at small forces (<200pN), k_{DLVO} is small and $k_{eff} \sim k_{DLVO}$. As a result, the measured force gradient on the virus is initially small at short indentations but asymptotes at large force to $k_{elastic}$ (Fig S1b-c). Thus, when the peak forces are less than ~200pN as in our case while scanning, the main contribution

to the repulsive gradient must be due to k_{DLVO} and only secondarily due to $k_{elastic}$. Furthermore, at these buffer conditions the adhesion force on the virus is very low and the van der Waals component of the DLVO force is small. Thus, the measured k_{eff} on the virus must arise primarily from electrostatic forces and secondarily from elasticity of the hydrated viral shell.

B. Theory of 0+1+2 multi-harmonic imaging and spectroscopy

Given the small amplitude oscillations and the fact that the tip senses the interaction forces for an appreciable part of the oscillation cycle (Fig. 1 main text), it is reasonable to assume a point mass model and subsume any effects related to the momentary excitation of higher eigenmodes(3, 4) into the η_{eff} term representing dissipation. Consider the equation governing tip motion $q(t)$ when it interacts with the sample:

$$\frac{\ddot{q}}{\omega_{far}{}^2} + q + \frac{1}{\omega_{far} Q_{far}}\dot{q} = \frac{F_{mag}\sin(\omega t) + F_{ts}(Z+q\ ,\dot{q})}{k_{cant}}$$
$$F_{ts}(Z+q\ ,\dot{q}) = F_{ts,CONS}(Z+q) + F_{ts,DISS}(Z+q,\dot{q}) \qquad \text{(S1)}$$

$q(t)$ is the tip motion due to cantilever deflection, k_{cant} is the equivalent stiffness of the (4)first eigenmode for which standard calibration methods exist, and F_{ts} is the tip sample-interaction force which is assumed to decompose additively into a conservative (tip-sample gap dependent) $F_{ts,CONS}$ and a dissipative (tip velocity dependent) component $F_{ts,DISS}$. We present this derivation for the case when the cantilever is directly driven (i.e. magnetically, thermo-mechanically or using Lorentz force) so that F_{mag} is the magnitude of the magnetic excitation force. Z is the difference between cantilever position and the sample, also known as the Z-piezo displacement (See Fig. S2). Furthermore, ω_{far}, Q_{far}, and k_{cant} are respectively the natural frequency, the quality factor and the calibrated stiffness of the fundamental mode of the cantilever, which are typically measured while the cantilever is withdrawn, or far from the sample.

Let the steady state motion of the tip interacting with the sample comprise of only the 0th, 1st and 2nd harmonics so that the tip displacement and velocity are

$$\begin{aligned} q(t) &= A_0 + A_1\sin(\omega t - \phi_1) + A_2\sin(2\omega t - \phi_2) \\ &= A_0 + A_1\sin(\theta) + A_2\sin(2\theta + 2\phi_1 - \phi_2) \end{aligned} \qquad \text{(S2)}$$

$$\dot{q} = A_1\omega\cos(\theta) + 2A_2\omega\cos(2\theta + 2\phi_1 - \phi_2)$$

assuming that these are the dominant harmonics that describe the motion, a fact that is readily observable from experiments in liquids. Since the tip motion is assumed to be periodic, so too must the tip-sample interaction force (from Eq. S1b) leading to the following Fourier expansion of the tip-sample interaction force in terms of its conservative and dissipative components:

$$F_{ts}(Z+q(\theta),\dot{q}(\theta)) = F_{ts} = F^0_{ts,CONS} + \sum_{n=1}^{\infty} F^n_{ts,DISS}\cos(n\theta) + \sum_{n=1}^{\infty} F^n_{ts,CONS}\sin(n\theta) \quad \text{(S3a)}$$

where

$$\begin{aligned} F^0_{ts,CONS} &= \frac{1}{2\pi}\int_0^{2\pi} F_{ts}\, d\theta \\ F^n_{ts,CONS} &= \frac{1}{\pi}\int_0^{2\pi} F_{ts}\sin n\theta\, d\theta \\ F^n_{ts,DISS} &= \frac{1}{\pi}\int_0^{2\pi} F_{ts}\cos\theta\, d\theta; n = 1..\infty \end{aligned} \quad \text{(S3b)}$$

In the intermittent contact regime, it can be shown that $F_{ts,CONS}(\theta)$ is *symmetric* about $\theta = 3\pi/2$ while $F_{ts,DISS}(\theta)$ is *antisymmetric* about $\theta = 3\pi/2$. As a result, while $F^1_{ts,CONS}$ is the 1st Fourier *sine* coefficient, the $F^2_{ts,CONS}$ on the other hand is the 2nd *cosine* coefficient since $\sin(\theta)$ and $\cos(2\theta)$ are both symmetric about $\theta = 3\pi/2$.

Substituting Eqs. (S2, S3) into (S1a) and balancing separately the constant, and the first two sine and cosine harmonic terms in the equation, readily leads to the following results that link the Fourier components of the interaction forces to the observables (cantilever harmonics amplitudes, and phases)(5). The n^{th} Fourier coefficient of the conservative interaction force is called the n^{th} *harmonic virial* and the n^{th} Fourier coefficient of the dissipative interaction force is called the n^{th} *harmonic dissipation*:

$$
\begin{aligned}
&(a)\quad F^{0}_{ts,CONS} = k_{cant}A_0 \\
&(b)\quad F^{1}_{ts,CONS} = -F_{mag}\cos(\phi_1) + k_{cant}A_1\left(1-\left(\frac{\omega}{\omega_{far}}\right)^2\right) \\
&(c)\quad F^{1}_{ts,DISS} = -F_{mag}\sin(\phi_1) + k_{cant}A_1\frac{\omega}{\omega_{far}Q_{far}} \\
&(d)\quad F^{2}_{ts,CONS} = k_{cant}A_2\left[\cos(2\phi_1-\phi_2)\left(1-\frac{4\omega^2}{\omega_{far}^2}\right)-\frac{2\omega}{\omega_{far}Q_{far}}\sin(2\phi_1-\phi_2)\right] \\
&(e)\quad F^{2}_{ts,DISS} = k_{cant}A_2\left[\sin(2\phi_1-\phi_2)\left(1-\frac{4\omega^2}{\omega_{far}^2}\right)+\frac{2\omega}{\omega_{far}Q_{far}}\cos(2\phi_1-\phi_2)\right]
\end{aligned}
\tag{S4}
$$

Consider now two important special cases of Eq. S4. Far from the sample, the natural frequency and quality factor of the fundamental eigenmode of the cantilever can be easily measured using a thermal tune in commercial AFM systems, and are denoted as ω_{far} and Q_{far} respectively. The direct excitation at a frequency ω must be tuned to exact resonance with $\omega = \omega_{far}$ with a steady state amplitude A_{1far} so that the tip motion $q_{far}(t)$ in the driven eigenmode, the phase lag of tip oscillation relative to the excitation ϕ_{1far}, and the magnitude of the magnetic driving force F_{mag} are given by:

$$
q_{far}(t) = A_{1far}\sin(\omega_{dr}t-\phi_{1far}),\quad \phi_{1far} = \frac{\pi}{2},\quad F_{mag} = \frac{k_{cant}A_{1far}}{Q_{far}} \tag{S5}
$$

Under these conditions Eq. (S4) then reduces to

$$
\begin{aligned}
&(a)\quad F^{0}_{ts,CONS} = k_{cant}A_0 \\
&(b)\quad F^{1}_{ts,CONS} = -\frac{k_{cant}A_{1far}}{Q_{far}}\cos(\phi_1) \\
&(c)\quad F^{1}_{ts,DISS} = \frac{k_{cant}A_{1far}}{Q_{far}}\left(\frac{A_1}{A_{1far}}-\sin(\phi_1)\right) \\
&(d)\quad F^{2}_{ts,CONS} = k_{cant}A_2\left[-3\cos(2\phi_1-\phi_2)-\frac{2}{Q_{far}}\sin(2\phi_1-\phi_2)\right] \\
&(e)\quad F^{2}_{ts,DISS} = k_{cant}A_2\left[-3\sin(2\phi_1-\phi_2)+\frac{2}{Q_{cant}}\cos(2\phi_1-\phi_2)\right]
\end{aligned}
\tag{S6}
$$

However for some soft cantilevers (typically triangular levers with short tips) in liquid environments, there is an important correction that needs to be taken into account in Eq. S6. For such cantilevers it is well known that the natural frequency ω_{near} and

quality factor Q_{near} of the cantilever located "near" the sample (say when the tip is located <50 nm from surface, within imaging distance) decrease significantly to $\omega_{near} < \omega_{far}$ and $Q_{near} < Q_{far}$ respectively due to hydrodynamic squeeze film that develops (6) between the cantilever and the sample surface. As a consequence of this important effect, the amplitude and phase of tip motion change relative to their values when the cantilever is withdrawn from the sample. The tip motion just before engaging the sample now becomes

$$q_{near}(t) = A_{1near}\sin(\omega_{dr}t - \phi_{1near}) \tag{S7}$$

with $A_{1near} < A_{1far}$ and $\phi_{1near} > \frac{\pi}{2}$. ω_{near} and Q_{near} can be measured by measuring the thermal spectrum after withdrawing the cantilever from the sample by a small distance (<50nm). Alternately, ω_{near} and Q_{near} can also be estimated by knowledge of the observables $\omega_{far,}\, Q_{far}, A_{1far}, \phi_{1far} = \frac{\pi}{2}, A_{1near}, \phi_{1near}$ as follows. When near the sample, we have the following relations from simple forced vibration steady state response theory

$$\frac{k_{cant}A_{1near}}{F_{mag}} = \frac{1}{\sqrt{\left(1-\left(\frac{\omega}{\omega_{near}}\right)^2\right)^2 + \left(\frac{\omega}{Q_{near}\omega_{near}}\right)^2}}; \qquad \tan(\phi_{1near}) = \frac{\left(\frac{\omega}{Q_{near}\omega_{near}}\right)}{\left(1-\left(\frac{\omega}{\omega_{near}}\right)^2\right)}$$

$$F_{mag} = \frac{k_{cant}A_{1far}}{Q_{far}}; \qquad \phi_{1far} = \pi/2 \tag{S8}$$

where F_{mag} is the magnitude of the magnetic excitation force. Using Eqs. (S8) it can be easily shown that the readily observable quantities A_{1near}, ϕ_{1near} are related to ω_{near} and Q_{near} as follows:

$$\begin{aligned} 1-\left(\frac{\omega}{\omega_{near}}\right)^2 &= \frac{A_{1far}}{A_{1near}Q_{far}}\cos(\phi_{1near}) = \frac{F_{mag}}{k_{cant}A_{1near}}\cos(\phi_{1near}) \\ \frac{\omega}{Q_{near}\omega_{near}} &= \frac{A_{1far}}{A_{1near}Q_{far}}\sin(\phi_{1near}) = \frac{F_{mag}}{k_{cant}A_{1near}}\sin(\phi_{1near}) \end{aligned} \quad . \tag{S9}$$

The key point is that both the amplitude and phase of the cantilever change as it is brought from "far" to within imaging distance of the sample ("near"), however this change is due to viscous hydrodynamic effects and must be separated systematically from the amplitude and phase changes that occur due to tip-sample interactions which

are discussed now. With this hydrodynamic correction for soft cantilevers in liquids with short tips, Eq. S4 becomes:

$$
\begin{aligned}
&(a)\quad F^{0}_{ts,CONS} = k_{cant}A_0 \\
&(b)\quad F^{1}_{ts,CONS} = \frac{k_{cant}A_{1far}}{Q_{far}}\left(-\cos(\phi_1)+\frac{A_1}{A_{1near}}\cos(\phi_{1near})\right) \\
&(c)\quad F^{1}_{ts,DISS} = \frac{k_{cant}A_{1far}}{Q_{far}}\left(-\sin(\phi_1)+\frac{A_1}{A_{1near}}\sin(\phi_{1near})\right) \\
&(d)\quad F^{2}_{ts,CONS} = k_{cant}A_2\left[\cos(2\phi_1-\phi_2)\left(\frac{4A_1}{A_{1near}}\cos(\phi_{1near})-3\right)-\frac{2A_1}{A_{1near}}\sin(\phi_{1near})\sin(2\phi_1-\phi_2)\right] \\
&(e)\quad F^{2}_{ts,DISS} = k_{cant}A_2\left[\sin(2\phi_1-\phi_2)\left(\frac{4A_1}{A_{1near}}\cos(\phi_{1near})-3\right)+\frac{2A_1}{A_{1near}}\sin(\phi_{1near})\cos(2\phi_1-\phi_2)\right]
\end{aligned}
\qquad \text{(S10)}
$$

In summary, both Eqs. S6 and S10 apply when the excitation frequency is tuned to the fundamental cantilever resonance far from the sample $\omega = \omega_{far}$. However, Eq. S10 applies when soft cantilevers with short tips are used so that the hydrodynamic effects must be considered and Eq. S6 may be used when the hydrodynamic squeezing effects are negligible.

Experimentally, one way to judge if hydrodynamic squeeze film effects are important or not is to do the following test with a magnetically or Lorentz force excited cantilever in liquid: First tune the excitation frequency to the fundamental resonance of the cantilever $\omega = \omega_{far}$ so that $\phi_{1far} = 90^{\circ}$ when the cantilever is withdrawn completely from the sample. Then with the excitation frequency fixed, approach the sample and observe the phase lag ϕ_{1near} just prior to when the amplitude and phase begin to change due to tip sample interactions. If $\phi_{1near} \sim 90-92^{\circ}$ then the hydrodynamic corrections are negligible but if $\phi_{1near} \sim 92-110^{\circ}$ then these corrections become very important.

In this work, for the Lorentz force excited cantilevers we typically excited them at $\omega = \omega_{far}$ so that $\phi_{1far} = 90^{\circ}$, however when close to the sample (just before the oscillating tip sensed the surface forces), $\phi_{1near} \sim 113-115^{\circ}$. Therefore, in this paper we had to use this hydrodynamic correction and Eq. S10 was used to convert the observables into the force harmonics. To convert the measured force harmonics into local material properties, consider the tip sample interaction model considered in the main text:

$$
\begin{aligned}
F_{ts} &= -F_{ad} - k_{eff}(Z+q) - \eta_{eff}\dot{q}, \textit{when } Z+q<0 \\
&= 0, \textit{otherwise}
\end{aligned}
\qquad \text{(S11)}
$$

We substitute $q(t) = A_0 + A_1\sin(\theta) + A_2\sin(2\theta + 2\phi_1 - \phi_2)$, $\dot{q} = A_1\omega\cos(\theta) + 2A_2\omega\cos(2\theta + 2\phi_1 - \phi_2)$ into (Eq. S11) and define $\delta_{max} = A_1 - Z - A_0$ is the maximum indentation into the sample so that $Z + q = -\delta_{max} + A_1(1+\sin\theta)$. We also denote a nondimensional indentation into the sample as $\Delta = \frac{\delta_{max}}{2A_1}$ so that when $0 < \Delta < 1$ the tip is intermittently tapping on the sample and $\Delta = 1$ implies permanent contact with the sample. In this case the tip is in contact with the sample whenever $Z + A_0 + A_1\sin(\theta) < 0$ or for $A_1(1+\sin(\theta)) - \delta_{max} < 0$ or for the duration $3\pi/2 - \cos^{-1}(1-2\Delta) < \theta < 3\pi/2 + \cos^{-1}(1-2\Delta)$. This equation form can be entered into the integrals described in Eq. (S3b) which can be exactly analytically evaluated in MAPLE to be as follows:

$$F_{ts}^0 = \frac{-F_{ad}(\pi - \arccos(-1+2\Delta)) + A_1 k_{eff}\left((1-2\Delta)(\arccos(-1+2\Delta) - \pi) + 2\sqrt{-\Delta(-1+\Delta)}\right)}{\pi}$$

$$F_{ts,CONS}^1 = -\frac{2F_{ad}(\pi - \arccos(-1+2\Delta)) + A_1 k_{eff}\left(\pi + 2(2\Delta-1)\sqrt{\Delta(1-\Delta)} - \arccos(-1+2\Delta)\right)}{\pi}$$

$$F_{ts,DISS}^1 = -\frac{A_1\eta_{eff}\omega\left(\pi + 2(2\Delta-1)\sqrt{\Delta(1-\Delta)} - \arccos(-1+2\Delta)\right)}{\pi}$$

$$F_{ts,CONS}^2 := \frac{2F_{ad}(-\pi + \arccos(-1+2\Delta)) + 2A_1 k_{eff}\left(-\frac{8}{3}\Delta + \frac{8}{3}\Delta^2\right)\sqrt{\Delta(1-\Delta)}}{\pi}$$

$$F_{ts,DISS}^2 := \frac{1}{3}\frac{A_1\eta_{eff}\omega\left(-\sin(3\arccos(-1+2\Delta)) + 6\sqrt{-\Delta(-1+\Delta)}\right)}{\pi} \qquad \text{(S12)}$$

Thus we use Eq. (S10) to convert the multi-harmonic amplitudes and phases into force harmonics, and Eq. (S12) to relate the force harmonics to the four unknowns – the material properties $F_{ad}, k_{eff}, \eta_{eff}$ and Δ.

A MATLAB code has been written that performs a nonlinear best fit of those values of $F_{ad}, k_{eff}, \eta_{eff}$ and Δ that best match the measured force harmonics in Eq. (S12). The code effectively solves nonlinear least-squares data-fitting problems by using a predefined starting point x_0 and finding a minimum of the sum of squares of the functions of interest. This code has been optimized to first interpret by using the topography data the HOPG substrate and the viral particle. This allows us to choose

clever boundaries conditions giving improvement of an order of magnitude in computational speed.

C. **Comparison of material properties extracted from multi-harmonic method vs. static force-distance curve**

Conventionally, the elastic stiffness on a virus is measured in the strongly repulsive regime of the virus F-Z (force-displacement) curve with forces around 1nN and indentation of ~8nm (Fig. S3a).(7-9) In multi-harmonic AFM of viruses in buffer solutions we have shown that this is not the case because we are applying very small peak forces <200pN to achieve optimal amplitude reduction to scan the sample. Thus as discussed in section A of this supplement, the effective physical properties $F_{ad}, k_{eff}, \eta_{eff}$ using multi-harmonic method corresponds to physical properties measured at a specific drive frequency indentation depth, and applied force.

In order to compare the estimated physical properties using the multi-harmonic dynamic AFM method with those extracted using conventional quasi-static force-distance curves, we made a careful statistical comparison of the two methods with other ϕ29 virions. F-Z curves were recorded on top of the virions and on HOPG using very slow speeds ~50nm/s, at the locations indicated by crosses in the 3D rendered topography image in Fig. S3a. Then the data were converted to F-d (force-gap) curves and a linear spring constant model for a sample was used to fit the curve. Fig. S3b and S3c are the F-d curve during approach on top of the virus shell and on the HOPG substrate, respectively. Superimposed to these curves is the schematic of the linear model, giving the broad idea of how the model really analyzes the data in terms of approach curves. In particular, in order to back out the effective properties from these curves, we restrict the fits to forces <200pN as encountered in the dynamic AFM experiments. This analysis has been performed on F-d curves acquired on the virus and HOPG yielding the following values; for virus k_{eff} =0.026N/m, and HOPG k_{eff} =0.11N/m and F_{ad} =251pN.

Histograms of k_{eff} on the virus and F_{ad} on the HOPG substrate maps Figs. S3(d-e) are shown in order to extract the distribution of values in the selected regions and compare them with the extracted values from the quasi-static F-d curves. Comparing both methods using the histograms we can observe that the extracted material properties from the methods of k_{eff} on the virus and F_{ad} on the HOPG substrate are within 1% and 10%, respectively. These results prove the high accuracy and precision of our proposed multi-harmonic dAFM method.

In order to compare both methods using a more rigorous statistical metric, the force gradients k_{eff} values has been obtained in a specific highlighted area in an image

containing four different bacteriophage ϕ29 viruses and presented in a histogram. Figures S4(a-d) are the topography images and material properties maps of the viruses extracted using the method described in the text. Usually histograms representation requires to fulfill the Sturges' rule which determines the width of the bars (i.e. bins) representing *a priori* indistinguishable events. Since the data respond to a normal distribution the histogram (Fig. S4 e-g) has been adjusted to a Gaussian distribution in order to know the most probable value of k_{eff}. In Fig. S4f are summarized the values of k_{eff} obtained from the Gaussian distribution and the mean $\pm$ SD (Standard Deviation) values obtained from different static F-d performed on each virus (A red, B green, and C blue color) and fitted in the low interaction regime used in dynamic AFM maps. We observe the values obtained from k_{eff} histograms are in agreement with the k_{eff} from static curves within the statistical error (Gaussian distribution). For example, the mean value for k_{eff} histograms of virus C is $0.023 \pm 0.004 N/m$ and k_{eff} extracted from static curves is $0.027 \pm 0.007 N/m$ showing a very small variation between both methods and this is expected from experimental uncertainties. Since the particles present the same absorption orientation on the HOPG surface and not structural damage is observed, it reasonable that all the probed particles present a similar comparison of k_{eff} between the two methods.

D. Data on additional viruses

In this work we conducted many AM-AFM imaging experiments of bacteriophage ϕ29 viruses and extracted their physical properties. In Fig. S5 we provide additional images taken with Lorentz-force excited cantilevers, showing that the multi-harmonic method can be easily implemented with repeatability and confidence yielding theexpected values at the imaging applied forces and indentations.

Further, we show two extra examples of the disruption of a phage ϕ29 and their physical properties and structure integrity variations. Figures S6 and S7 show the analysis of two different progressive steps in the disruption process of the virus shown in Figs. 2 and 3 from the main text after performing the nanoindentation experiments. Both images (Figs. S6 and S7) show a superposition of icosahedral network of protein trimers on the 3D topography images in order to check the progressive disruption on the virus structure. In addition, we show the differences in topography and physical magnitudes as adhesion, stiffness and viscosity before and after particle damage in both cases. Figures S6(b-e) and S7(b-e) are shown in order to observe and track the differences in topography and material properties. After performing the first nanoindentation by applying an average normal force of approximately 500 pN, the virion has started to be disrupted by eliminating a trimer. A profile performed on the intact part of the shell (Fig. S6a) shows that there is small decrease in height provoked

by an initial volume decrease of about 7%. After a second nanoindentation, reaching a force of ~800 pN the structural damage increases on areas close to the the initial rupture place. The neighboring trimers have been critically affected, although still there are unaffected shell areas at the bottom of the virus structure. Consequently, there is a decrease in height ~10 nm and a decrease in total volume of ~28% (Fig. S7a). This reinforces the conclusion that part of the packed DNA is lost from the virion after puncturing.

Figures S6(c-e) and S7(c-e) show that after the removal of trimers, $\Delta\eta_{eff}$ decreases and propagates to regions which are not correlated with the damaged topography (see the profiles in Figs. S6f and S7f). On the other hand, ΔF_{ad} and Δk_{eff} do not show any significant net change, agreeing with the observations proposed in the main text.

E. Preparation of figures in the main text and supplement

In the main text, Fig. 3 has been smoothed and equalized to improve image contrast. First the images have been equalized to saturate the substrate to get the best possible contrast on the virus. Then a 2 point Gaussian smoothing filter has been applied to the data to remove noise. Image color has been changed to gray scale because this one shows better detail within the virus. Finally improvement of light using the 3D rendering has been done.

In Figs. 5, S6, and S7 in order to generate maps of changes in material properties and topography we calculate the difference on the before and after damage shell image. For image presentation an equalization procedure has been done followed by a 2 point Gaussian smoothing. Raw data was used for line profiles generation done on different location on the virus particle topography and physical magnitude maps. An important step to mention for this analysis is the superposed icosahedral network of protein trimers on the virus. In order to do that in a systematic and free of error way we draw the mesh on top of the viral shell using the 3D topography image and in order to identify unique features to perform the best fit.

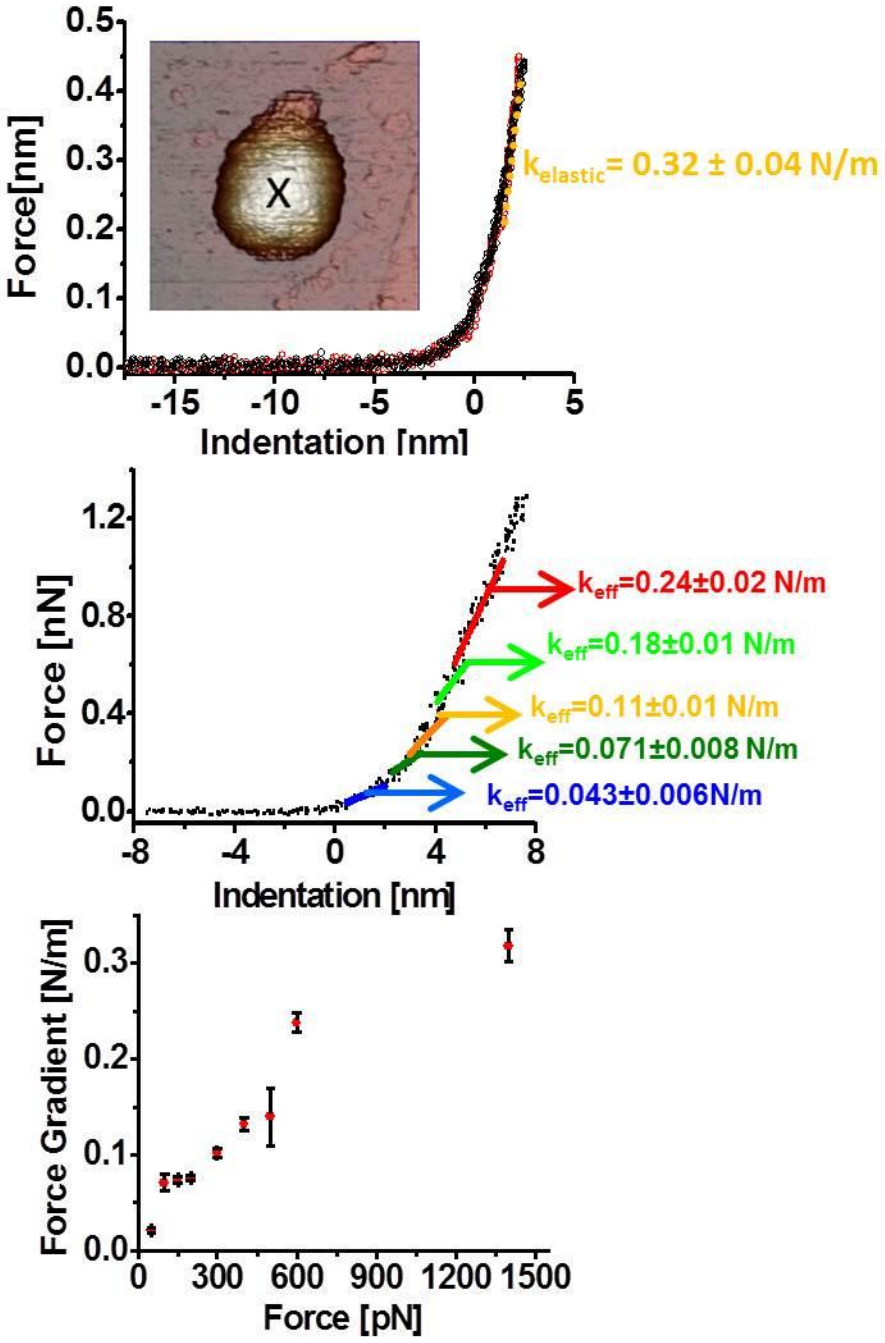

Figure S1. a, Force vs. indentation ($\delta = -d$) forward (black) and backward (red) curves acquired on top of a ϕ29 virion, with an asymptotic slope (repulsive gradient) of 0.32 N/m corresponding to $k_{elastic}$. **b**, linear fits of the same curve as in (a), demonstrating the variation of k_{eff} as a function of max force, and **c,** plot of k_{eff} as a function of the force at which the gradient is calculated. The error bars are defined by the standard deviation and they are based on 5 different measurements at the same point.

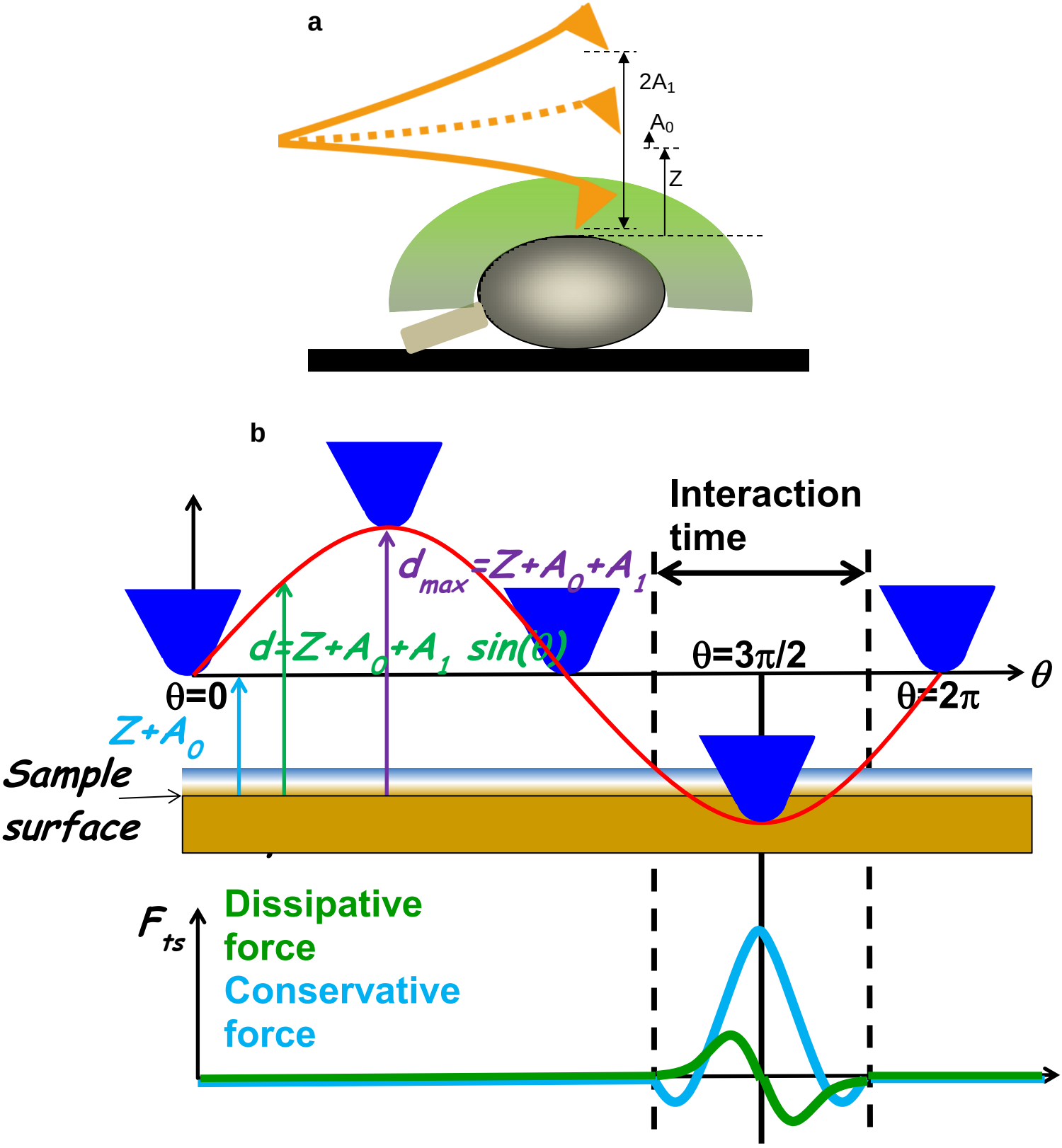
a
2A1
A0
Z
b
Interaction time
dmax=Z+A0+A1
d=Z+A0+A1 sin(θ)
θ=0
θ=3π/2
θ=2π
θ
Z+A0
Sample surface
Fts
Dissipative force
Conservative force

Figure S2. **a,** A schematic of an oscillating cantilever showing the key motion/displacement variables. The schematic emphasizes that while operating in liquids it becomes necessary to account for the average deflection of the tip A_0, which is generally comparable to the setpoint amplitude of the drive harmonic A_1. **b,** A schematic shows the time history of tip motion (in terms of θ) to leading order, along with the conservative and non-conservative tip-sample interaction forces encountered by the tip during this motion.

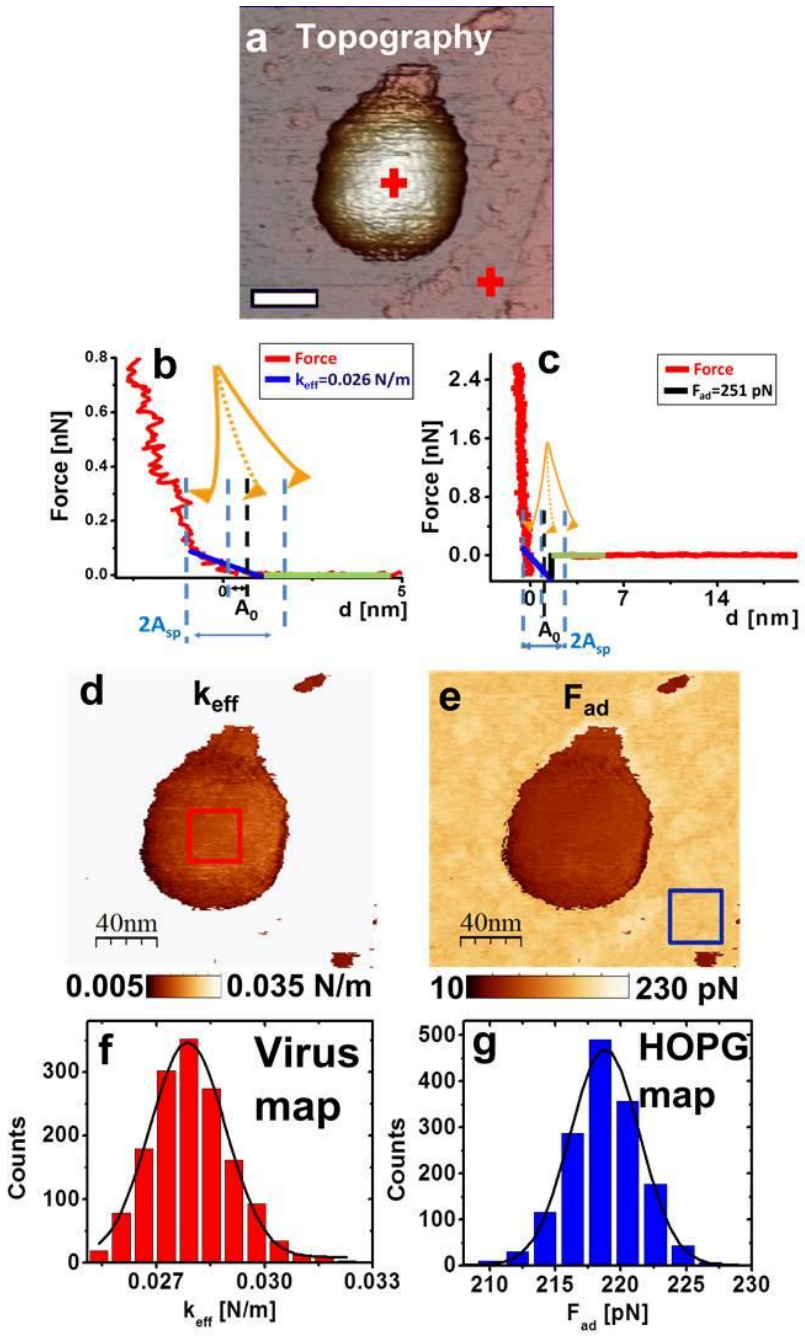

Figure S3. **a**, Topography image of the bacteriophage ϕ29 presented in Figs. 2 and 3 of the main text. **b and c,** are quasi-static F-d curves extracted from a F-Z curve on top of the virus shell and on HOPG, respectively, at points shown by the crosses in (a). The cantilever dynamics as the AFM tip is brought to contact on the virus and the HOPG has been superimposed on the curves to highlight the differences when interacting with different sample surfaces. **d and e,** Images of the material properties maps k_{eff} and F_{ad} of the sample derived from the multi-harmonic observables as described in the main text. **f and g,** Histograms showing the distribution of the k_{eff} and F_{ad} from a specific area of interest on the material property maps.

Cartagena, Hernando-Pérez et al

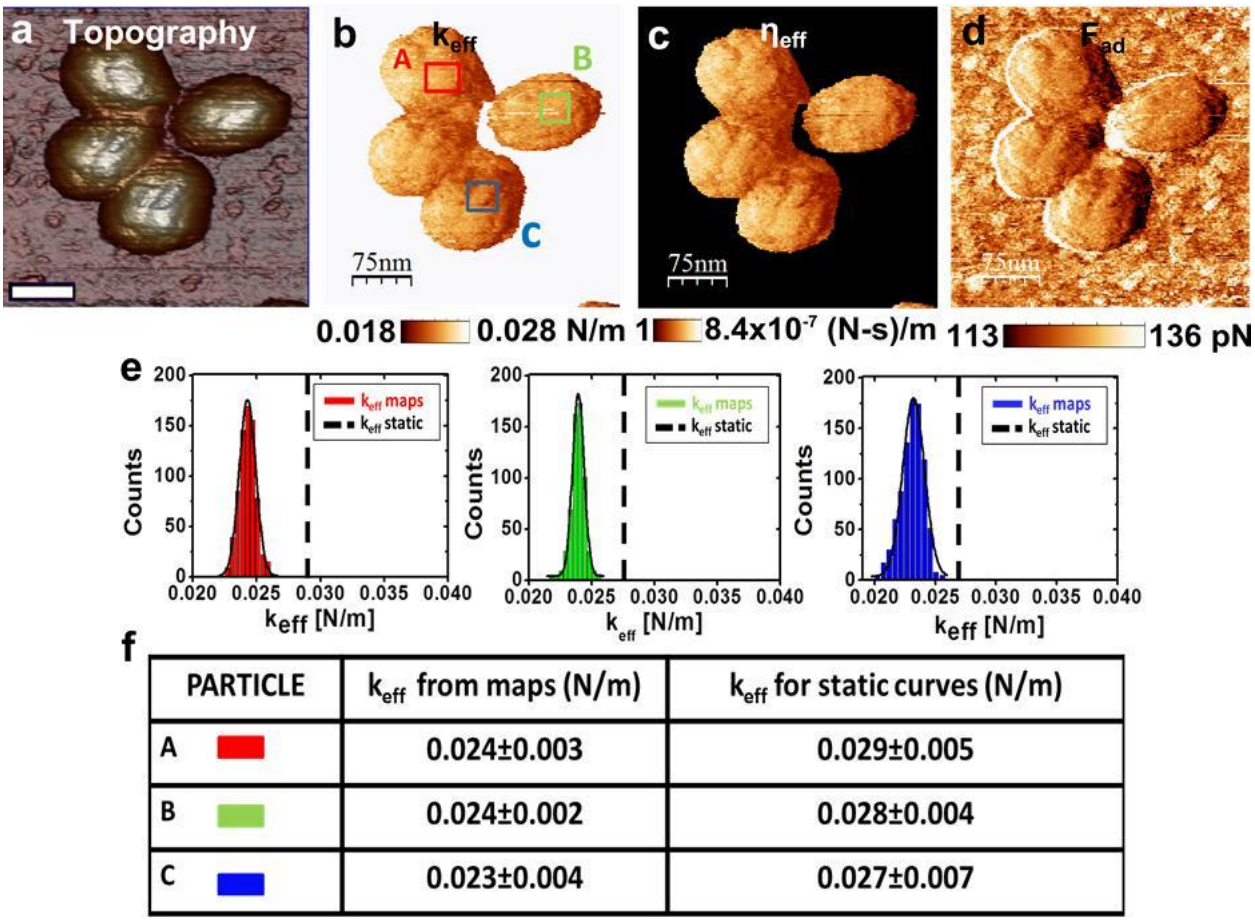

PARTICLE	k_{eff} from maps (N/m)	k_{eff} for static curves (N/m)
A	0.024±0.003	0.029±0.005
B	0.024±0.002	0.028±0.004
C	0.023±0.004	0.027±0.007

Figure S4. a, Topography image of multiple ϕ29 viruses. **b-d,** Material property maps: effective stiffness k_{eff}, intrinsic viscosity η_{eff}, and adhesion force F_{ad} derived from the multi-harmonic observables as described in the main text. **e,** Histograms showing the distribution of the k_{eff} of different ϕ29 viruses marked with a color square. Dashed line is the mean value of k_{eff} obtained from repeated quasi-static force-distance curves on the same location. **f,** Table containing the summary of stiffness value distributions using multi-harmonic and static-distance curves methods.

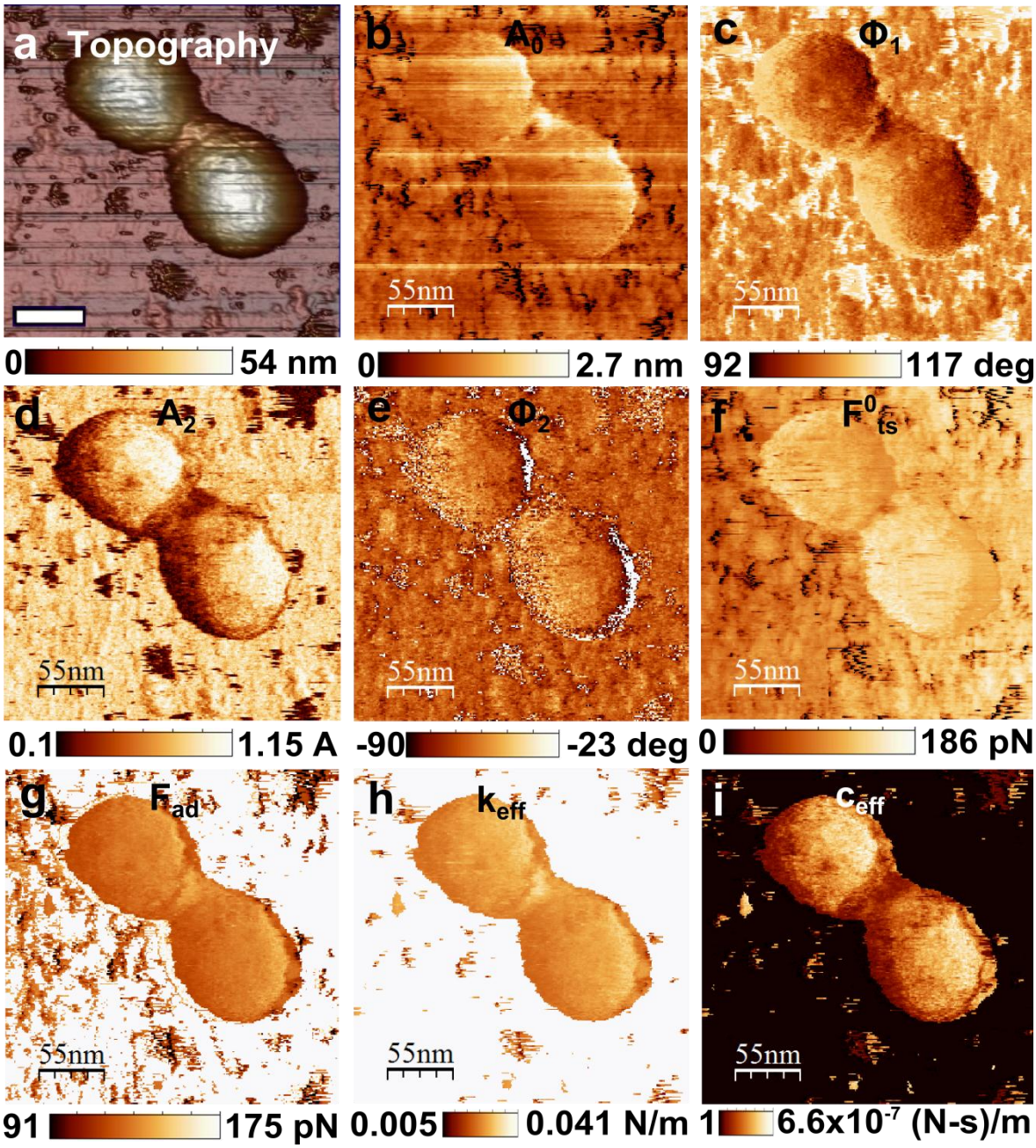

Figure S5. Additional bacteriophage ϕ29 virus extracted material property maps. **a,** 3D rendered topography image of a bacteriophage ϕ29 using a Lorentz excited TR400 microcantilever showing two well defined virions. **b-e,** Multi-harmonic data (A_0, ϕ_1, A_2, ϕ_2) recorded simultaneously with topography. **f,** Is the applied force map F_{ts}^0 at which the imaging was done during the experiment. **g-i,** Maps of the local material properties: adhesion force (pN), local effective stiffness (Nm^{-1}), and effective viscosity (Nsm^{-1}), respectively.

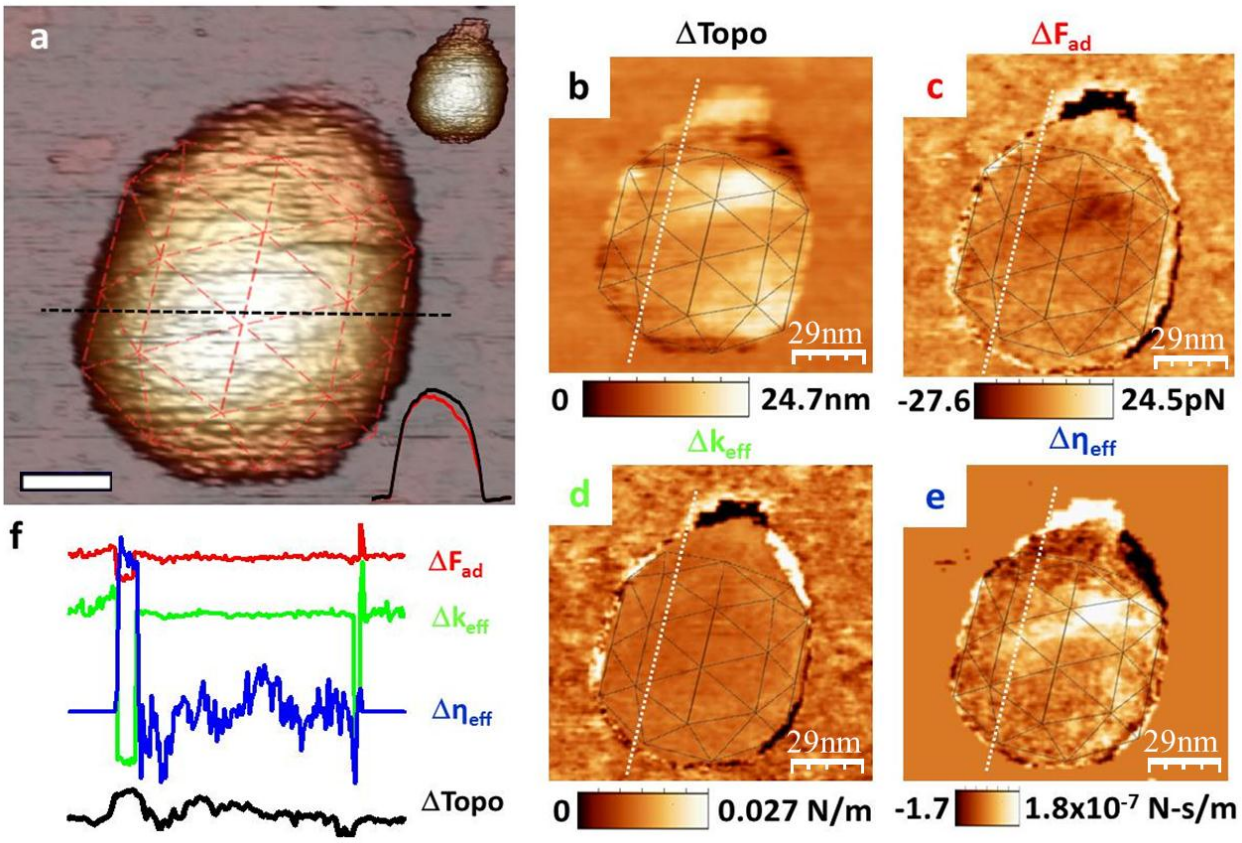

Figure S6. **a,** 3D topography image of a disrupted bacteriophage ϕ29 with superposed icosahedral network. **b,** Difference of topography map, **c,** adhesion map, **d,** effective stiffness map and **e,** effective viscosity map before and after shell damage, respectively. **f,** Longitudinal axis profile of material properties differences along the viral shell (white dash lines). Profile of effective viscosity map present a behavior that does not correlate with the topography and the other material properties. Insets: is the 3D rendered topography image for the intact virus and the height profile comparison before (black), and after (red) particle damage.

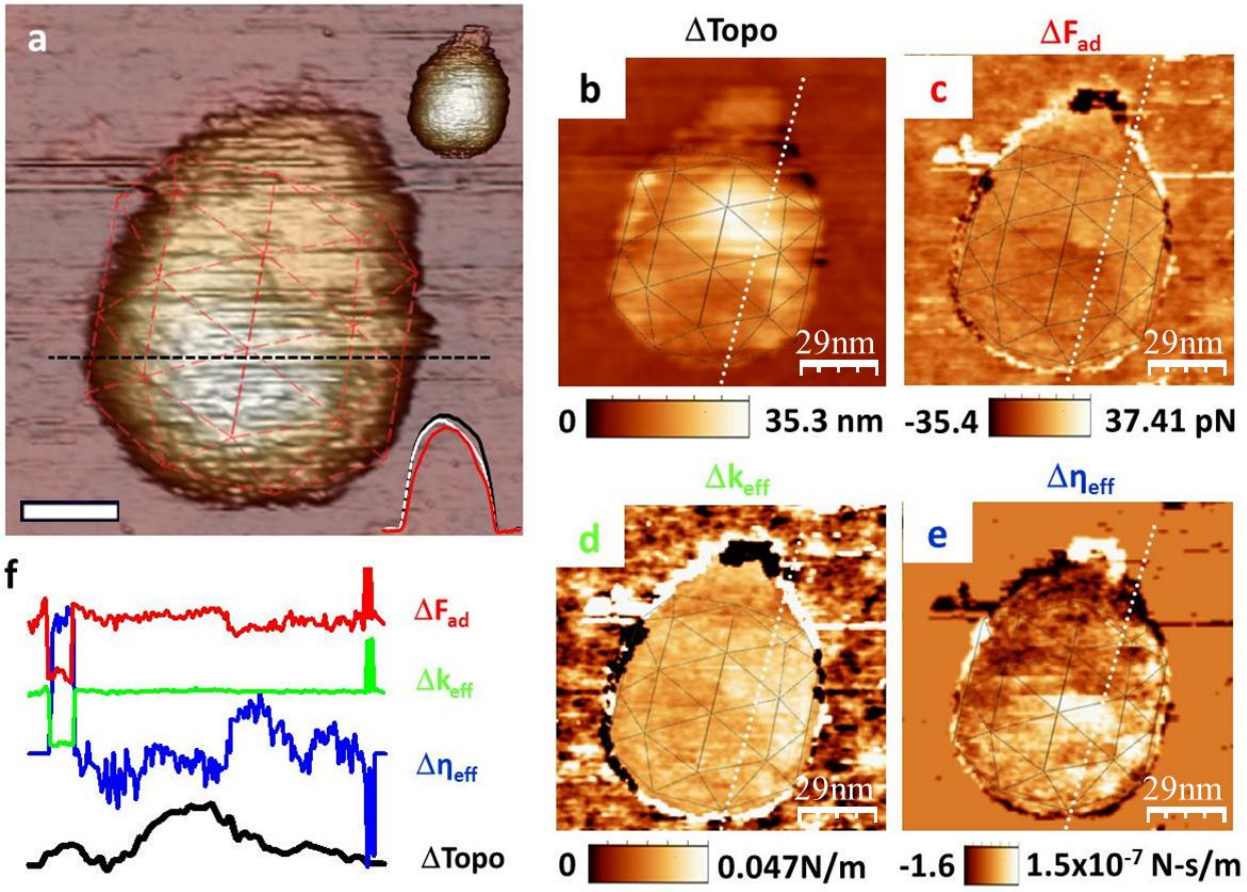

Figure S7. **a,** 3D topography image of progressive disruption bacteriophage ϕ29 with superposed icosahedral network. **b,** Difference of topography map, **c,** adhesion map, **d,** effective stiffness map and **e,** effective viscosity map before and after a progressive shell damage, respectively. **f,** Longitudinal axis profile of material properties differences along the viral shell (white dash lines). Profile of effective viscosity map present a behavior that does not correlate with the topography and the other material properties. Insets: Is the 3D rendered topography image for the intact virus and the height comparison intact virus (black), after first damage (dashed white) and after progressive damage (red).

References for supplementary material

1. Evilevitch A, Roos WH, Ivanovska IL, Jeembaeva M, Jonsson B*, et al.* (2011) "*Effects of Salts on Internal DNA Pressure and Mechanical Properties of Phage Capsids"*Journal of Molecular Biology **405,** 18-23.
2. Evilevitch A, Fang LT, Yoffe AM, Castelnovo M, Rau DC*, et al.* (2008) "*Effects of salt concentrations and bending energy on the extent of ejection of phage genomes"*Biophysical Journal **94,** 1110-1120.
3. Melcher J, Carrasco C, Xu X, Carrascosa JL, Gomez-Herrero J*, et al.* (2009) "*Origins of phase contrast in the atomic force microscope in liquids"*Proceedings of the National Academy of Sciences of the United States of America **106,** 13655-13660.
4. Basak S & Raman A (2007) "*Dynamics of tapping mode atomic force microscopy in liquids: Theory and experiments"*Applied Physics Letters **91**.
5. Raman A, Trigueros S, Cartagena A, Stevenson APZ, Susilo M, Nauman E, *et al.* (2011) "Mapping nanomechanical properties of live cells using multi-harmonic atomic force microscopy" Nature Nanotechnology **6**, 809-814.
6. Xu X, Carrasco C, de Pablo PJ, Gomez-Herrero J & Raman A (2008) "*Unmasking imaging forces on soft biological samples in liquids when using dynamic atomic force microscopy: A case study on viral capsids"*Biophysical Journal **95,** 2520-2528.
7. Roos WH, Gertsman I, May ER, Brooks CL, Johnson JE*, et al.* (2012) "*Mechanics of bacteriophage maturation"*Proceedings of the National Academy of Sciences of the United States of America **109,** 2342-2347.
8. Carrasco C, Castellanos M, de Pablo PJ & Mateu MG (2008) "*Manipulation of the mechanical properties of a virus by protein engineering"*Proceedings of the National Academy of Sciences of the United States of America **105,** 4150-4155.
9. Michel JP, Ivanovska IL, Gibbons MM, Klug WS, Knobler CM*, et al.* (2006) "*Nanoindentation studies of full and empty viral capsids and the effects of capsid protein mutations on elasticity and strength"*Proceedings of the National Academy of Sciences of the United States of America **103,** 6184-6189.